SUPPORTING INFORMATION

Details of Superresolution Imaging Method

The initial concentration of the active YFP/yGFP fluorophores inside the cell is far too high for single molecule imaging. Moerner and coworkers (Biteen *et al.*, 2008) showed that YFP can be used for superresolution imaging by first photobleaching the entire sample, after which some 10-20% of the non-fluorescent molecules gradually return to a fluorescent state. The photobleaching pulse of 514 nm light (4 kW/cm^2 at the objective for 10-20 s) was applied once to each cell. Immediately after the pulse, the rate of return of YFP molecules to the fluorescent state is too high for single-molecule imaging, especially in the case of S2-YFP with its large copy number. Eventually, the cells exhibit only a few (0-3) fluorescent puncta. Even long after the photobleaching pulse, new fluorescent copies continually appear during the observation time. This may be caused in part by gradual maturation of YFP-containing species as the cells grow and divide.

In the subsequent localization and tracking movies of S2-YFP, different laser intensity was used for measuring ribosome spatial distributions vs ribosome diffusion properties. In both cases, we used 30 ms camera frames (33 Hz frame rate) with 15 ms exposure time within each frame. To obtain superresolution images of the time-averaged ribosome spatial distribution, we used a stronger beam of 514 nm light (2 kW/cm^2 at the objective) to provide bright single-molecule images with fast bleaching. Under these conditions, we typically localized some 1200-3000 molecules per cell over some 7000-10,000 camera frames. We collect one image per 30 ms over an interval of 3-4 min, after which time the rate of appearance of new molecules has become very low. The molecules fluoresce for only 1-3 frames at this high intensity. Ribosomes move rather slowly. With 15 ms exposure times, typical single molecules yield fluorescence spread over roughly a 3 px x 3 px region, essentially a diffraction-limited spot.

Single-molecule tracking of ribosomes was carried out using a lower intensity of the 514 nm laser (0.5-1 kW/cm^2 at the objective). In these conditions, we collect some 100-200 photons per molecule per frame and the average trajectory length increases to 5-6 frames. Trajectories were collected from each cell over a period of 10-15 min (20,000-30,000 frames). In that time we typically observe 500-1500 single molecules whose trajectories comprise some 5000-7000 localizations. Typically particles in 1-4 cells were tracked simultaneously to enhance the efficiency of data collection. For the tracking analysis, we have separated single cells into set of movies for each cell. For mean-square displacement (MSD) analyses of ribosome diffusion, we chose to include only longer trajectories to improve accuracy over longer lag times. In practice we varied the cutoff time scale for each cell. The lower limit on trajectory length was chosen in the range 8-13 steps so that at least 40–60 trajectories are included for each cell. Trajectories longer than the cutoff for each cell were truncated at the cutoff value.

In principle it would be possible to space the camera frames more widely in time and observe the manner in which the MSD plots approach an asymptote at long times. In practice, we could not arbitrarily lengthen the time between frames due to the nature of the YFP imaging. The photobleaching laser pulse converts all molecules to a dark state. After conversion, a small fraction of the dark molecules become fluorescent again. However, we cannot control the rate at which they return. If frame spacing is chosen too long, too many molecules are fluorescent in

each frame. Moreover, there are limits on the total laser dosage the cell can endure while maintaining an unperturbed DNA and ribosome spatial distribution; see below.

In the usual ribosome tracking movies, we found no evidence of rapidly diffusing species such as S2-YFP or bare YFP. However, it might be argued that rapidly diffusing molecules would make blurred images that are not detected by the superresolution thresholding algorithm for 15-ms exposure times. Could the tail on the measured distribution be due to free S2-YFP or YFP copies that happen to diffuse slowly enough to be detected? To test this possibility, we plotted the spatial distribution of only the "faster" molecules in Fig. 6 and found it to be segregated into three ribosome-rich regions like the "slower" molecules. Based on Kaede and YFP superresolution images, we would expect free S2-YFP or YFP copies to be homogeneously distributed throughout the cytoplasm. In addition, we imaged S2-YFP using 4-ms exposure times appropriate for such rapid diffusion (Bakshi et al., 2011). There was no change in the ribosome spatial distributions. Finally, the distribution of 2-step mean-square displacements from the 4-ms movies remained consistent with $D \sim 0.04\ \mu m^2\text{-}s^{-1}$; there was no evidence of diffusion at $\sim 5\ \mu m^2\text{-}s^{-1}$. The absence of free S2-YFP suggests that the cell does not make a substantial excess of S2 relative to the number of 30S subunits.

The yGFP label is used for superresolution imaging by reversible photobleaching here for the first time. The number of β'-yGFP copies per labeled-RNAP cell is a factor of 10 smaller than the number of S2-YFP copies per labeled-ribosome cell. For the RNAP-yGFP studies, we used 1-3 kW/cm^2 of 514 nm light at the objective both for bleaching (0.5-1.0 min) and for imaging (60-ms frames with 30 ms exposure time within each frame). We rejected frames with too many single molecule images (more than 4 particles per cell). We typically detect some ~400 photons per molecule per frame, and the mean trajectory length is 3-4 frames.

Numerical test of the precision of centroid fitting

Determination of particle position by calculating the centroid of the fluorescent spot rather than fitting the distribution to a Gaussian function requires justification by numerical simulation. This is especially true in view of an earlier numerical study that found large systematic error and poor localization accuracy from a centroid algorithm (Cheezum *et al.*, 2001). However, the Cheezum study used an 80 x 80 pixel grid to calculate the centroid and did not apply a high-pass spatial filter to the image. This meant that the numerous pixels far from the image spot have tremendous leverage in the centroid. In contrast, our method smooths and filters the image first, yielding a fluorescent spot that lies in a roughly 5 x 5 grid of pixels. We use an 8 x 8 grid to calculate the centroid. Most of the pixels near the edge of the grid have values near zero, so they do not unduly bias the centroid value. We prefer centroid estimation to Gaussian fitting because diffusing molecules make non-circularly symmetric images, centroid calculation is very fast, and the results are easily compared with Monte Carlo calculations of diffusion.

To estimate the accuracy of centroid vs Gaussian fitting for ribosomes in our imaging conditions, we simulated random walks of a particle with $D = 0.04\ \mu m^2\text{-}s^{-1}$ on a square lattice with 5 nm spacing between points. At each time step of 0.171 ms, the particle moves 0 or ±1 step to left or right and 0 or ±1 step up or down. For each random walk, a 170-step trajectory was formed to match the experimental 30 ms/frame. Each position was blurred with a two-dimensional Gaussian of $\sigma_{x,y} = 75$ nm, closely approximating the point spread function using a NA = 1.49 objective at $\lambda = 560$ nm. The sum of the 170 broadened images was used to represent

a 30 ms/frame image of a single, diffusing ribosome. The images were re-binned into a 20 x 20 pixel images with 100 nm pixels, matching experiment. Two noise components were also added: shot noise with $\sigma_{shot} = n^{1/2}$, where n is the number of photons in the pixel, and a background noise contribution chosen from a Gaussian distribution with $\sigma_{background}$ varied to achieve different peak signal-to-noise ratios (PSNR). The PSNR is defined as the peak signal pixel value divided by the standard deviation of the background, $(\sigma_{background}^2 + \sigma_{shot}^2)^{1/2}$.

In Fig. S15, we show example simulated images for PSNR = 6 and 11; the relevant range for our experiments is 8-15. The adjacent images have been smoothed and filtered as for experiment, removing much of the background. Analysis of the particle locations was performed in the same way as for the tracking data from experiment. The localization results for one particular random walk trajectory with PSNR = 6 and 11 are shown for the two algorithms, centroid and Gaussian fitting, in Fig. S15 A,B. Each *x-y* graph covers a 200 nm x 200 nm region at the sample. The true particle centroid of the random walk on the fine grid is shown as a '+' at the center of the region. For that one random walk, we carry out 100 realizations of the shot noise and background noise and locate the particle using the centroid calculation and the symmetric Gaussian fitting on the 8 x 8 pixel grid. The resulting localizations are shown as the dots. Systematic errors are modest for both methods, as evidenced by the symmetric placement of dots about the central +. For a diffusing particle, each trajectory has its own peculiar shape. To assess the effects of the variable shape of trajectories, we did the same analysis for 10 unique trajectories. The localization precision using Gaussian fitting vs centroid calculation are compared in Fig. S15D as a function of PSNR. For PSNR = 6-17, the precision (standard deviation) of the centroid algorithm varied from 33 nm to 10 nm. In the manuscript, we use the conservative estimate σ = 30 nm in each dimension. The standard deviation is 10-15% higher for the centroid calculation vs Gaussian fitting at each PSNR. Unlike the Cheezum result, the centroid algorithm does not fail catastrophically at modest PSNR. Presumably Gaussians are somewhat more precise in this example because the diffusion coefficient is small enough to create fairly round images. We suspect, but have not shown, that centroid fitting may be preferred in cases of more severe blurring due to faster diffusion, where the images become more asymmetric.

Extent of ribosome-nucleoid segregation for multiple cells

The superresolution distribution of S2-YFP labels for 17 cells was examined to determine the degree of segregation. We normalized the distribution of each cell and plotted intensity vs *relative* axial coordinate, where 1 is the full tip-to-tip cell length. These normalized profiles are plotted on a false color scale (Fig. S2A). The maxima consistently appear at the center and at the end caps, as is also obvious from the widefield images. One such profile is graphed in Fig. S2B. The regions between the end cap peaks and the middle peak generally drop to 10-30% of the maximum. The mean fractional density for the left dip in this study was 0.21± 0.13, and for the right dip was 0.28±0.13. Sectioning by the 1.49 NA objective limits ribosome detection to a central slab of 500-600 nm height, smaller than the measured 780 nm cytoplasmic diameter.

Calculation of copy number of protein constructs

Following Taniguchi et al. (Taniguchi *et al.*, 2010) we have calculated the copy number of the protein constructs (ribosome-YFP or RNAP-yGFP, Fig. S6) by dividing the total intensity in the first camera frame by the mean intensity of a single molecule. In converting total intensity in

frame one to the ribosome or RNAP copy number, the total intensity must be corrected for a small contribution of autofluorescence and for differences in camera gain and laser intensity between the two measurements. The autofluorescence contribution is estimated at ~1-2% for ribosome images and ~10% for RNAP, based on wild type cells imaged under the same conditions. We also apply a small, 10% correction for the presence of immature YFP copies that go undetected; see the simple kinetic analysis below. The total intensity in the first frame is obtained with the laser intensity attenuated 20-fold and 2X shorter exposure time to avoid photobleaching during that frame. The single molecule images are obtained at the usual intensity. We have calibrated the camera gain in the two imaging conditions.

We have tested that the YFP fluorescence intensity under single-molecule imaging conditions is the same for the original copies as for the "revived" copies that return to a fluorescent state over minutes after photobleaching. For this test to work, we needed only a few hundred original copies per cell, so we used a cell line expressing the fusion protein HU-YFP from a plasmid inducible by tetracycline. Due to strong binding to DNA, HU-YFP has a diffusion coefficient D_{HU} of about 0.05 μm^2-s^{-1}, comparable to the ribosomes under study. Our strategy was to create small copy numbers of original fluorescent molecules by imaging cells in the absence of inducer. In practice, cells initially exhibited 200-500 original fluorescent copies, far fewer than the YFP-labeled ribosomes or RNAPs. When the 514 nm laser is turned on continuously, the original copies photobleach very rapidly. After several seconds, only a few or no fluorescent YFP copies are observed. Then some 20-50 photobleached copies gradually return, typically over a time period of several minutes. By measuring single-molecule intensities over the period 3-10 s after the laser is turned on, we obtain an intensity histogram that is due primarily to copies in the original fluorescent population. We also require these copies to be located within an earlier clump of fluorescent species that have mostly photobleached, i.e., not to appear suddenly on a dark background as revived copies would. Then we continue to measure single-molecule intensities over the subsequent two-minute period and make a second histogram, this time including only molecules that appear suddenly on a dark background.

The two histograms of integrated camera counts from original vs revived copies state are compared in Fig. S16. The distribution dominated by original copies has a mean of 104 ± 40 arbitrary intensity units (± 1σ). The distribution of revived copies has a mean of 106 ± 49 arbitrary intensity units. The good agreement strongly suggests that revived copies have the same photophysical properties in the cytoplasm as original copies.

Creating a binary mask and cell outline from the white light images

Simple white light images obtained with the 1.49 NA objective are used for determining the cell outline. We have used available thresholding algorithms and developed our own algorithm to generate cells masks and outlines from the low contrast white light images. The principal axes of these images become the *x*, *y* coordinate system used in plotting spatial distributions.

Before image processing the white light images (Fig. S9A) are inverted by subtracting all the pixel values from the maximum pixel value. In this format the cell appears as a bright object on a dark background (Fig. S9B). Then we make a preliminary binary mask of the cell using a threshold. The threshold is determined by the Matlab function 'greythresh', which utilizes Otsu's method (Otsu, 1979) of computing the threshold. We then use the Laplacian and Gaussian (LoG) algorithm of edge detection, as explained by Silusarenko, *et al.* (Sliusarenko *et al.*, 2011). This image is saved as Image1 (Fig. S9C). The inverted image created from the original image is then

used to create another filled mask. We use the Sobel method of edge detection by determining the locations of maximum gradient of intensity (default algorithm in MATLAB's "edge" function). Then we dilate the image using the Matlab function 'imdilate'. Finally the holes in this image are filled (a hole is set of isolated background pixels) to create the filled mask Image2 (Fig. S9D). By combining the Image1 (edge detection) and Image2 (filled mask) together using the AND operation, we generate the final mask (Fig. S9E). This mask is used for determining principal axes of the cell to compute the necessary rotation matrix to place images of different cells along the same axes. The outline of this mask can be simply by the outermost pixels of the mask (Fig. S9F).

Measuring cell doubling time for plated cells

In a bulk culture, the doubling time of a construct is obtained by measuring optical density (OD) vs time. To estimate doubling times for plated cells under our imaging conditions, we have used phase contrast images to measure cell length vs time, both in the flow chamber and in coverslip-slide sealed chambers. We used a phase contrast objective (NA = 1.30) to create time-lapse movies of 50-ms frames with 18-sec intervals for 200 frames (60 min). These images were analyzed using Matlab. The inverted phase contrast image was used to create a binary mask outlining each cell. Masks for many cells were created and separated with connected component analysis (Rosenfel.A & Pfaltz, 1966). For each binary mask, the major axis length and the centroid of the region were determined. The length of the major axis is taken as the cell length. For following the growth of individual cells in a sequence of frames, the centroids in successive frames are compared. Using the Delaunay triangulation method, we determine the nearest neighbors in successive frames and call them the same cell. This allows for movement of cells and microscope stage drift over 60 min. We fit plots of cell length vs time to the function:

$$L(t) = L_0 \cdot 2^{t/t_{1/2}} \qquad \text{(S1)}$$

Here the usual doubling time is $t_{1/2}$ and the initial cell length is L_0. The base-*e* time constant for growth used in the main text and in the kinetics scheme below is $\tau_g = t_{1/2}/\ln 2 = 1.44\ t_{1/2}$. An example data set is shown in Fig. S10. In chambers the strains grow 15% slower than the hot air shaker.

Effects of laser illumination on DNA and ribosome distribution

For the superresolution spatial distributions of S2-YFP and β'-yGFP, images were typically obtained at 3 kW/cm^2 of 514 nm light on the sample for periods of 2-3 min. For the single-molecule tracking experiments we used 0.5-2 kW/cm^2 over a longer period of 10-15 min. We inadvertently discovered that still higher laser exposure alters the spatial distribution of ribosomes and of DNA and also alters the diffusive properties of ribosomes. For example, after 10 min of 514 nm illumination at 6 kW/cm^2, both ribosome and DNA distributions become much more homogeneous, and the mean ribosome mobility appears faster than in unperturbed cells. This is reminiscent of the behavior on treatment with rifampicin, but we do not understand the mechanism behind this process. Similar effects were observed at 561 nm. See Fig. S12.

Kinetics scheme for cell growth and YFP maturation

Here we use Y to denote the number of immature, non-fluorescent copies of YFP and Y* to denote the number of mature, fluorescent copies. The overall rate constant for exponential

growth of cells is k_g. The base-e rise time for exponential cell growth is $\tau_g = k_g^{-1}$; the more usual "doubling time" is $t_{1/2} = \tau_g/\ln 2 = 1.44\ \tau_g$. The unimolecular rate constant for YFP maturation is k_{mat}. The simplest kinetics scheme assumes that the total rate of production of new YFP copies in the culture is proportional to the current total population, (Y + Y*). This amounts to assuming that as cells grow exponentially, the total YFP population is proportional to total cellular mass. Production and maturation of YFP is then governed by the simple equations:

$$dY/dt = k_g(Y + Y^*) - k_{mat}Y \quad \text{(S2)}$$

$$dY^*/dt = k_{mat}Y \quad \text{(S3)}$$

In exponential growth, the ratio Y / Y* should be constant:

$$Y^* = cY \quad \text{(S4)}$$

Thus $$dY/dt = c\,dY^*/dt \quad \text{(S5)}$$

Combining (S2), (S3), and (S5) yields the result:

$$k_g c^2 + (k_g - k_{mat})c - k_{mat} = 0 \quad \text{(S6)}$$

whose solution is: $$c = k_{mat}/k_g \quad \text{(S7)}$$

Thus $$Y^* = (k_{mat}/k_g)\,Y = (\tau_g/\tau_{mat})Y \quad \text{(S8)}$$

Imaging ribosomes in cells immobilized on agar coating

To test for possible effects of the polylysine coating on the coverslips on the observed ribosome distribution, we imaged cells sandwiched between a clean coverslip (treated with acetone and then KOH) and a thin pad made from 1% agar in EZRDM buffer. An example image is shown in Fig. S17. These images are qualitatively similar to the widefield images acquired from cells plated on polylysine.

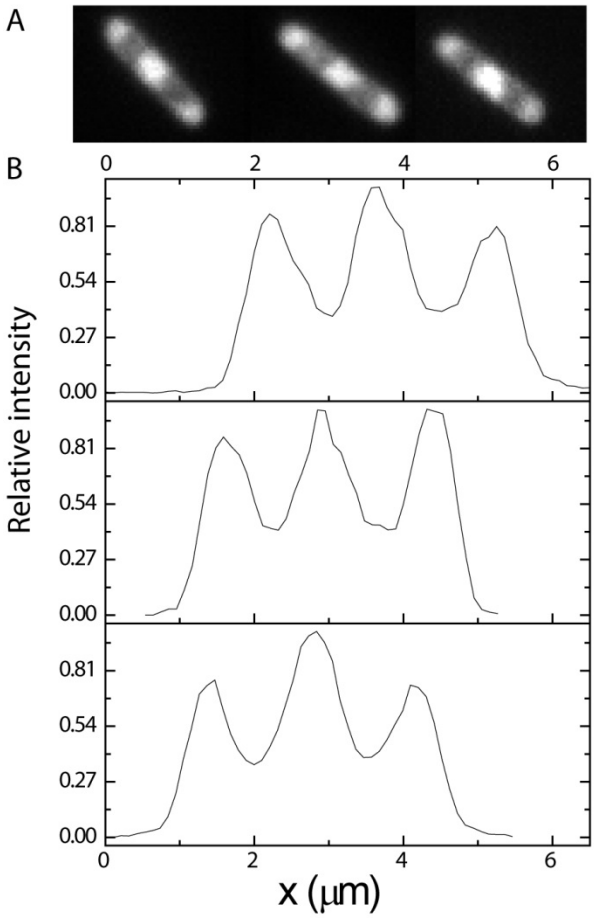

Figure S1. (A) Widefield images of ribosomes (S2-YFP) taken with 1.25 NA objective. (B) Axial intensity profiles of ribosome distributions showing larger peak-to-valley ratios (2.0 to 2.5) than those from the 1.49 NA objective (Fig. 1).

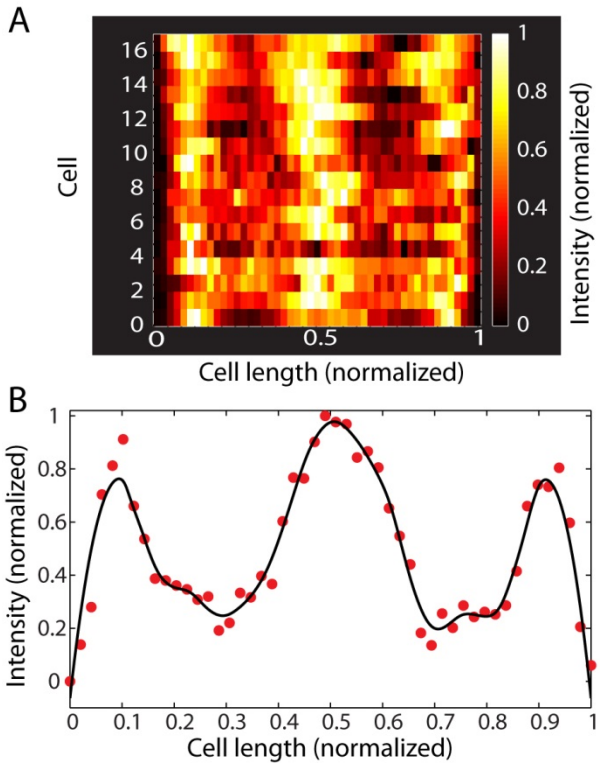

Fig S2. (A) Distribution of ribosomes along the long axis of the cell for 17 cells is plotted as relative intensity vs relative position and color coded. (B) Axial profile for one example cell.

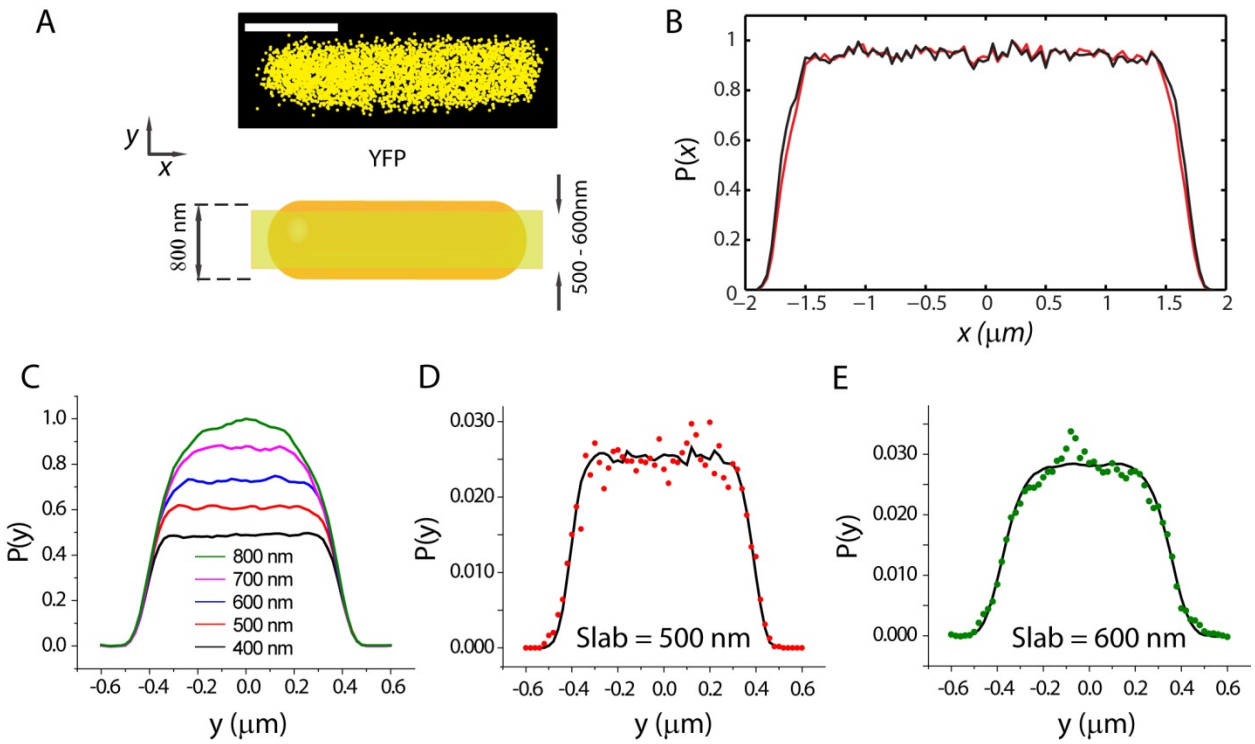

Figure S3. Sectioning by 1.49 NA objective. (A) Super-resolution image of free YFP distribution in live *E. coli* (projection onto *xy* plane). Scale bar is 1micron. Diagram shows sectioning along *z* by 1.49 NA objective. Single-molecule detection is most sensitive to molecules in a central slab of 500-600 nm thickness. (B) Monte Carlo distribution of projections onto *x*-axis for randomly distributed locations within a spherocylinder of diameter 760 nm and cell length L = 3600 nm, including endcaps. Black: no sectioning. Red: Detection only in a 500 nm thick slab (z = ±250 nm). Sectioning has little effect on axial distribution. (C) Monte Carlo distribution of projections onto *y*-axis for sectioning slabs of varying thickness as shown. Endcaps are excluded from these distributions. (D) Experimental distribution of P(y) for free Kaede molecules; (Bakshi *et al.*, 2011). The best-fit model curve uses the 500-nm thick slab and radius R = 400 nm. (E) Experimental P(y) for free YFP. Best-fit model curve uses the 600-nm thick slab and radius R = 380 nm. The thickness of the detection slab may vary with single-particle signal-to-noise ratio, diffusion coefficient, and tuning of the intensity threshold for localizing a single molecule. We conclude that for S2-YFP, detectability is best for molecules in a slab of 500-600 nm thickness.

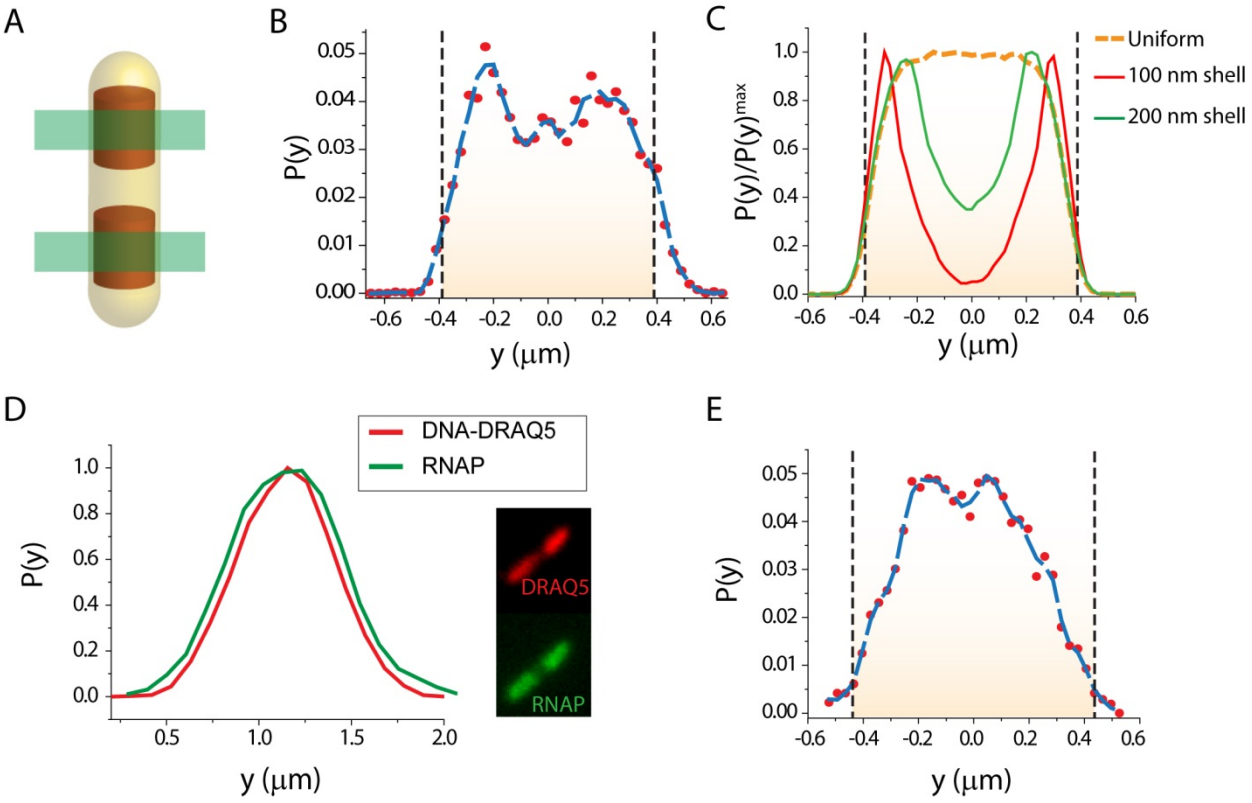

Figure S4. (A) Schematic of the two regions of *x* (green swaths) proximal to the dense nucleoid regions (brown cylinders) within which the *y*-distributions of ribosomes (S2-YFP) and RNAP (β'-yGFP) are analyzed. (B) Ribosome distribution P(*y*) projected onto the *y*-axis. Because there are few ribosomes proximal to the nucleoid, this is a composite of data from 12 cells. There is some broadening of the width due to slight misalignment of images of multiple cells. Dashed lines at ±390 nm show the mean radius of MG1655 cells. (C) Simulated radial distributions from distributions in a shell of thickness 100 nm (red line) and 200 nm (green line) is compared with uniform distribution (dotted orange line) with 600 nm detection slab. (D) For widefield imaging, the transverse distribution of RNAP (green curve) is broader than that of DRAQ5-DNA (red curve) from the same cell. (E) RNAP distribution P(*y*) from a single cell. Dashed lines at ±430 nm represent the mean radius of VH1000 cells, obtained from the Kaede distribution.

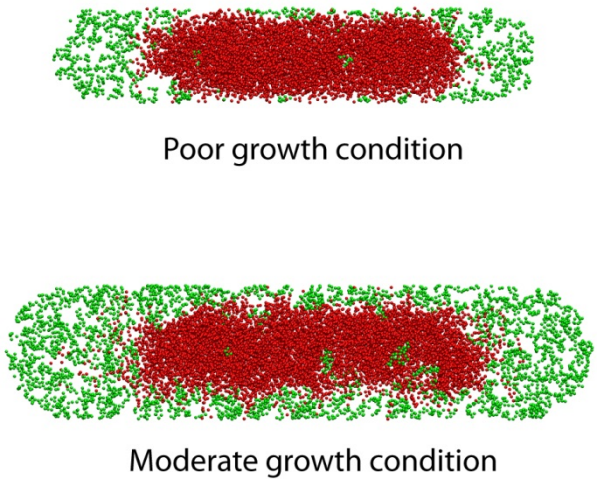

Figure S5. Model plectonemic DNA (red) and polysome (green) spatial distributions from Monte Carlo simulations published earlier (Mondal *et al.*, 2011). The model includes entropic and excluded volume effects, but no attractive forces.

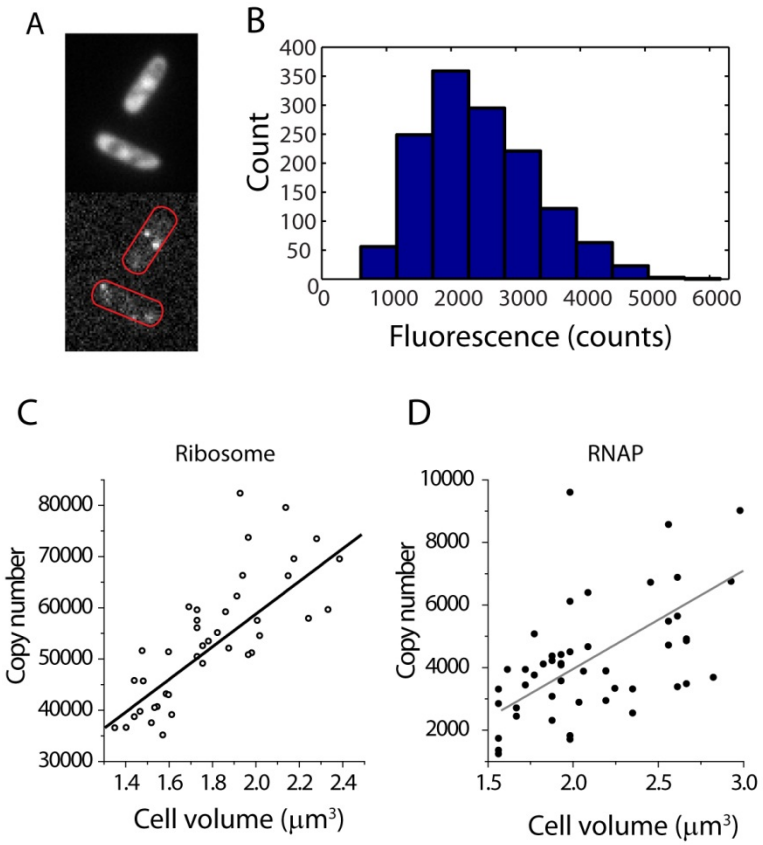

Figure S6. (A) Ribosome (S2-YFP) images by widefield (top) and superresolution method (bottom) of the type used to calibrate the single-molecule intensity. (B) Distribution of single-molecule intensities in camera counts. The mean of this distribution, when properly scaled for laser intensity and detector gain, is used to estimate the total number of fluorescent YFP copies per cell in the widefield images. (C) Ribosome copy number per calculated cell volume. (D) RNAP copy number per calculated cell volume. All data obtained in EZRDM at 30ºC.

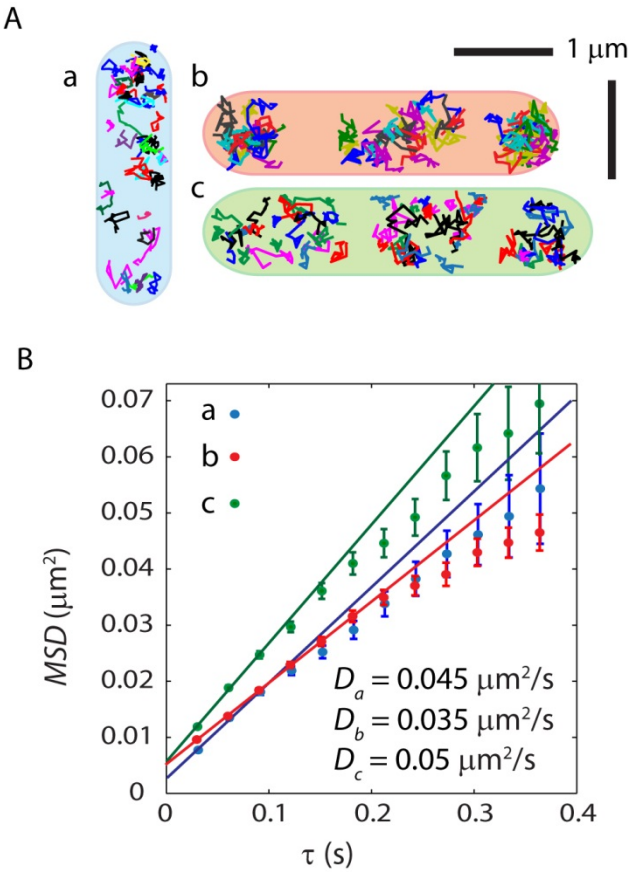

Figure S7. (A) Examples of ribosome trajectories for (a) short, (b) medium, and (c) long cells. (B) Mean-square displacement along *r* vs lag time τ averaged over all trajectories of 13 steps or longer from the same three cells. Solid lines represent straight-line fit to the first three data points in each case. Estimated diffusion coefficients from these lines are shown.

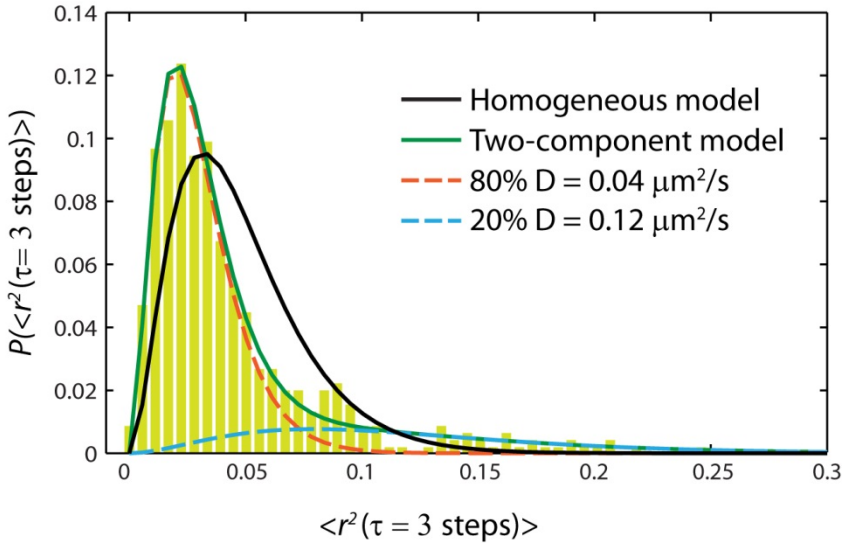

Figure S8. Histogram of 3-step MSD_r for combined ribosome data from 3 cells. Black line shows distribution for homogeneous free diffusion using $D = 0.05$ μm^2-s^{-1}, which corresponds to the mean of the experimental MSD_r values. Green line shows an example of a fit to a two-component distribution with 80% $D = 0.04$ μm^2-s^{-1} and 20% $D = 0.12$ μm^2-s^{-1}. The fit is far from unique, but is useful for a rough description of the heterogeneity.

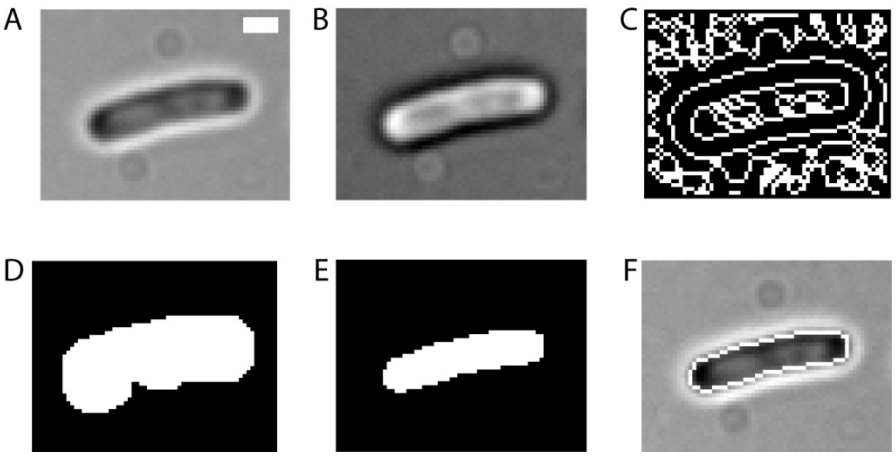

Figure S9. Steps of image processing to create the mask from a white light image from the cell. Scale bar =1 μm

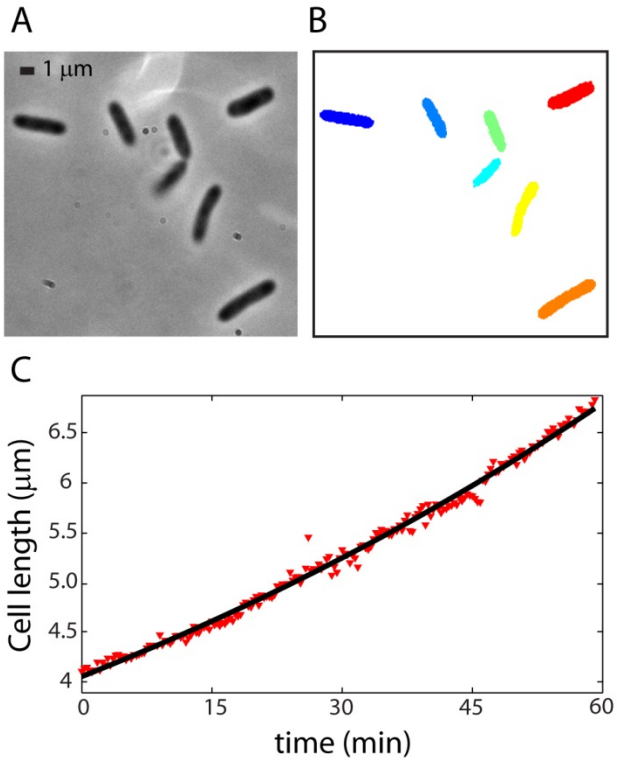

Figure S10. (A, B) Phase contrast images of 7 cells (scale bar 1μm) and the corresponding binary mask used to define the (x,y) coordinate system and measure cell length. (C) The major axis length for the binary mask of the left-most cell (dark blue) is plotted over 200 frames taken at 18-s intervals. Solid line is a fit to Eq. S1 to obtain the doubling time $t_{1/2}$ = 75 min.

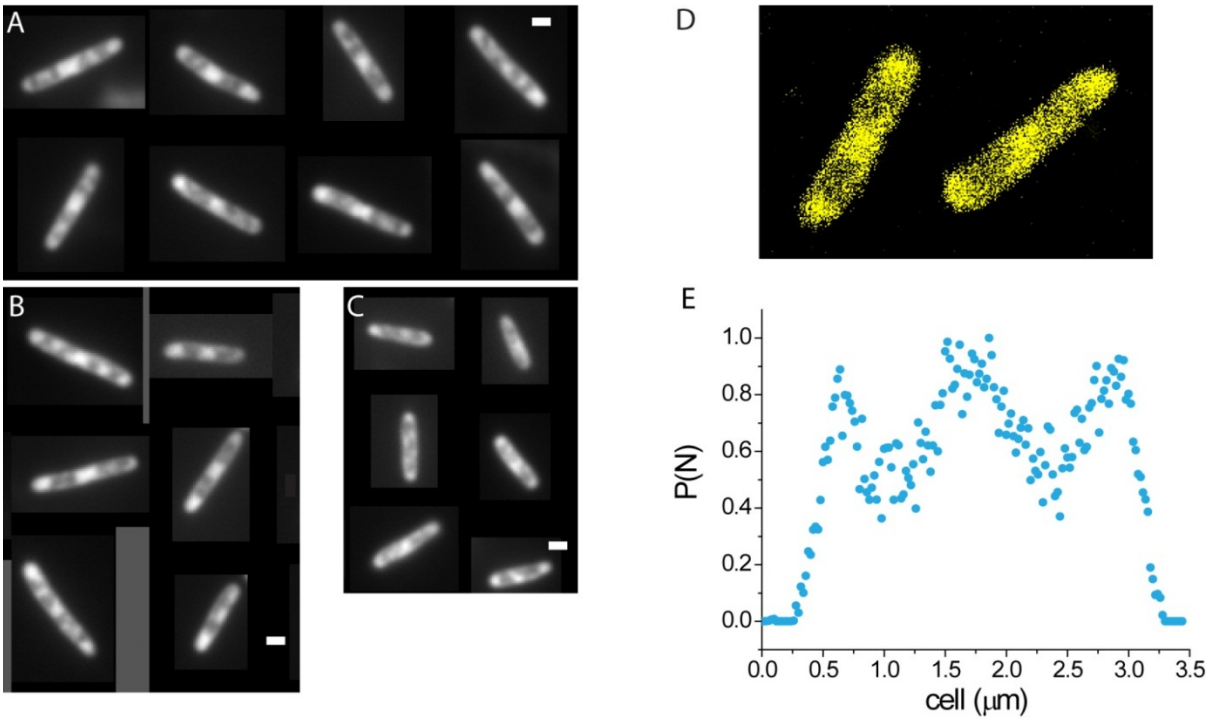

Figure S11. Examples of widefield ribosome (S2-YFP) images for *E. coli* cells growing in three different media. All images are taken at 30ºC. (A) Neidhardt defined complete medium, EZRDM. (B) Luria broth, LB. (C) Minimal MOPS-buffered medium, MBM. Bulk culture doubling times are 30 min, 55 min, and 87 min, respectively. Scale bar =1 μm. (D) Superresolution ribosome (S2-YFP) image of two cells grown in minimal MBM. (E) Axial ribosome distribution for a cell grown in minimal MBM.

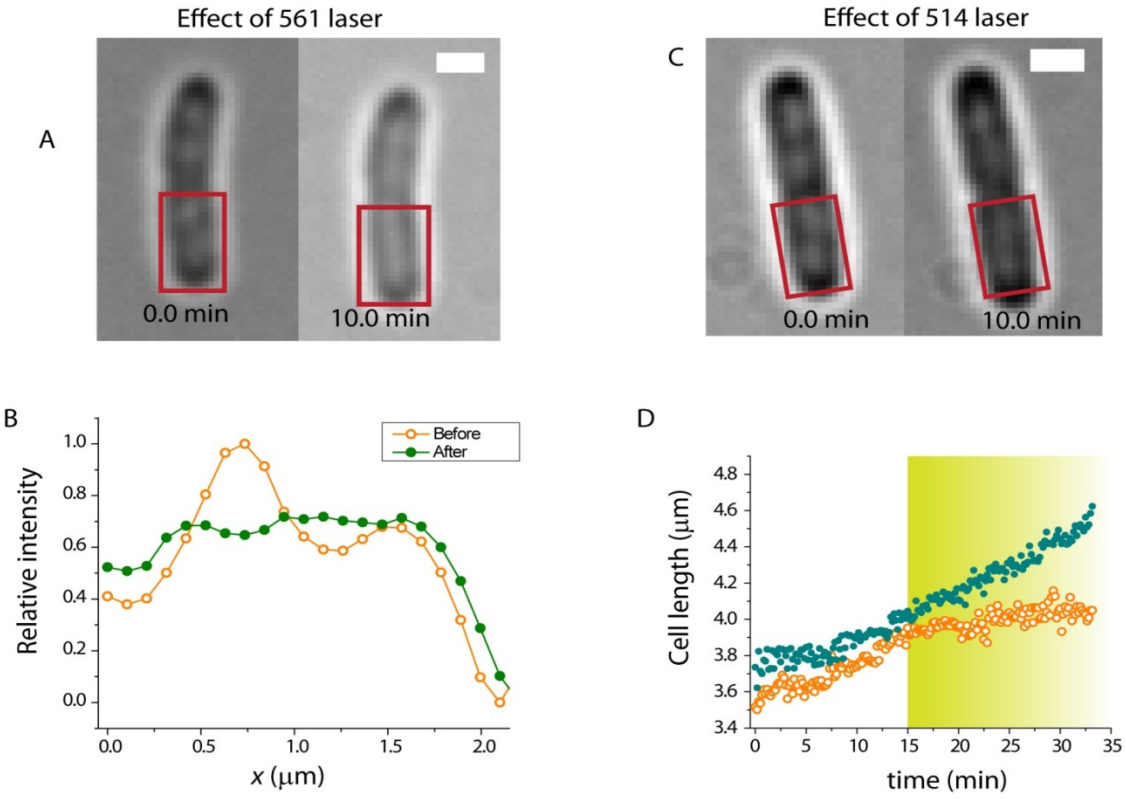

Figure S12. Laser effects. White light image of a cell clearly indicates the distribution of nucleoid as the lighter sections in a cell image. (A) White light image of WT cells before and after illumination at 561 nm at 7 kW/cm^2 for 10 min. Rectangle highlights one nucleoid sub-lobe that seems to fuse due to the laser treatment. (B) Axial white light intensity within the rectangle before and after illumination. (C) White light image of WT cells before and after 10-min illumination at 514 nm (6 kW/cm^2). (D) Cell length vs time for two cells from the same imaging area. One cell (orange data) was illuminated by the 514 nm laser at 6 kW/cm^2 while the other cell was not. The laser was turned on at t = 15 min, at which time growth of the illuminated cell slows immediately. Scale bar =1 μm.

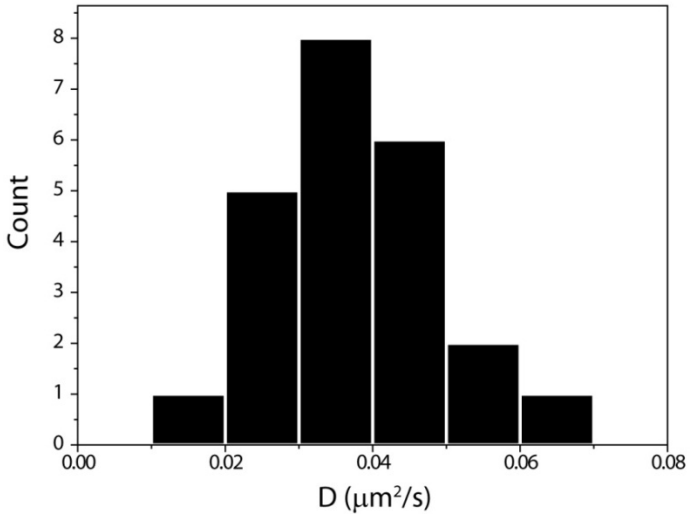

Figure S13. Distribution of diffusion constant of ribosome from 23 cells.

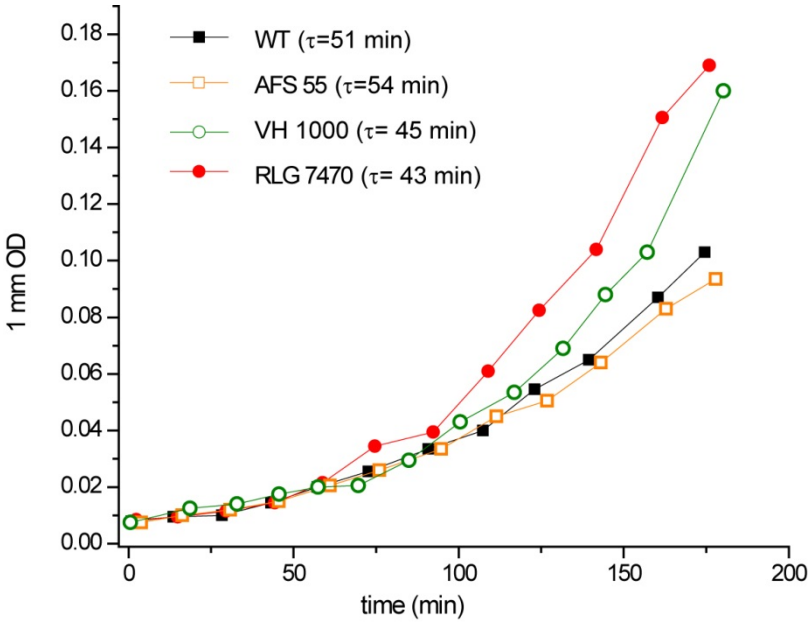

Figure S14. Growth curves at 30ºC for the strains expressing ribosome-YFP (AFS55) and RNAP-yGFP (RLG7470) are compared with wild type cells of MG1655 (background of AFS55) and VH1000 (background of RLG7470).

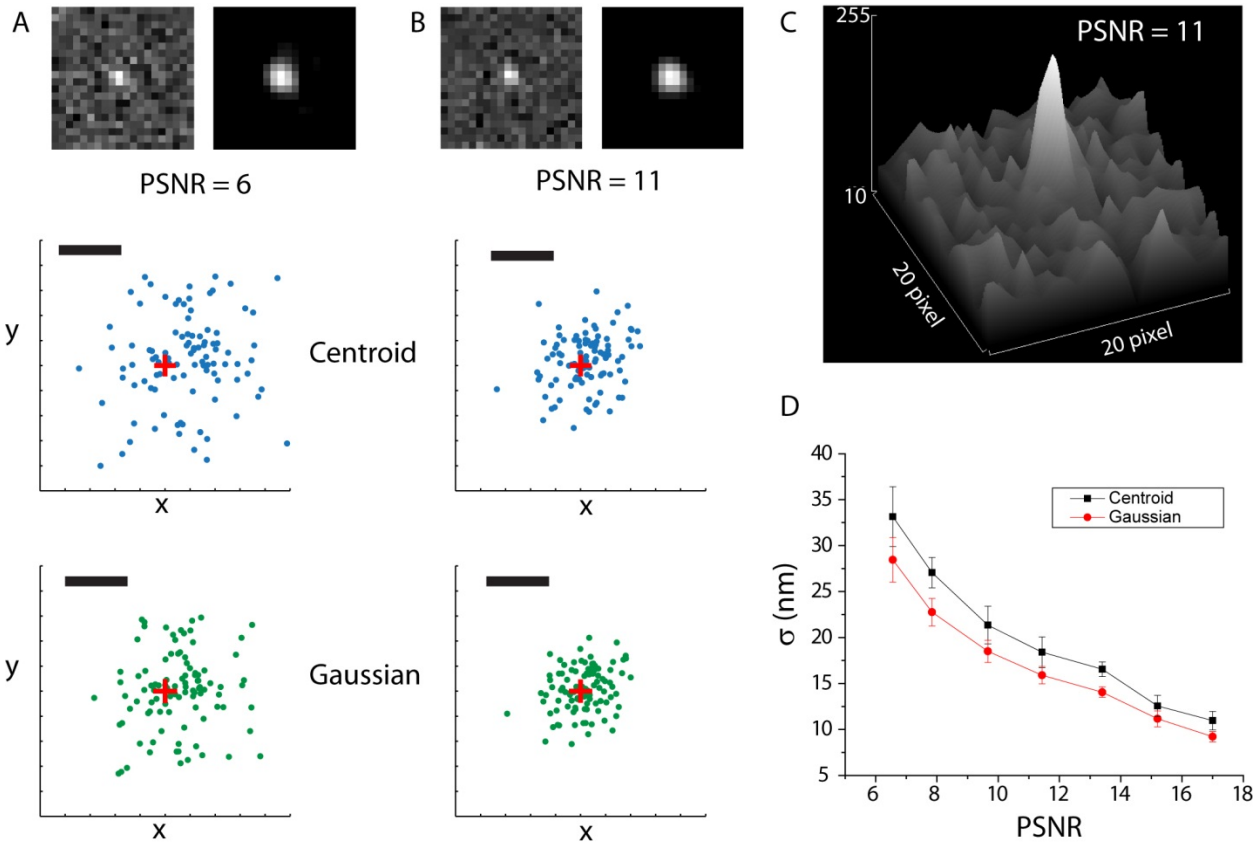

Figure S15. Top panel shows two simulated 2 μm x 2 μm single-molecule images (20 x 20 camera pixels) with PSNR 6 and 11 (left: raw image, mimicking camera frame; right: filtered and smoothed). The *xy* plots show the un-pixellated localization results for 100 realizations of noise for the same trajectory, obtained by applying the centroid calculation (middle panel) or Gaussian fitting (lower panel) to the filtered and smoothed image. The red '+' is the exact centroid of the true trajectory. Scale bar = 50 nm. (C) Intensity levels for an image with PSNR = 11 is shown for the 20 x 20 pixel region around the peak. (D) Mean localization precision (1 standard deviation) vs PSNR is shown from 10 simulated trajectories at each PSNR, comparing Gaussian fitting and centroid algorithm. Error bars represent one standard deviation of the distribution of localization precisions.

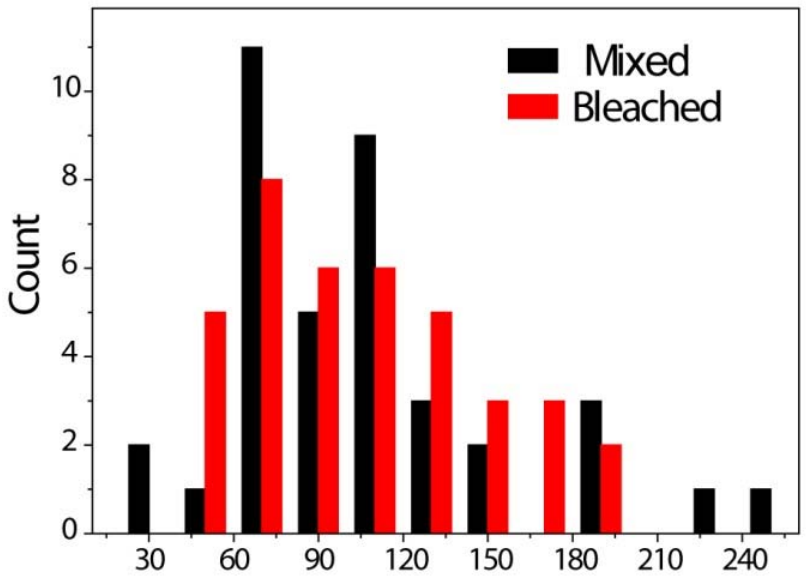

Figure S16. Comparison of photon count from reversibly bleached ("revived") HU-YFP and a mixed population of mostly original, unbleached HU-YFP plus some revived HU-YFP.

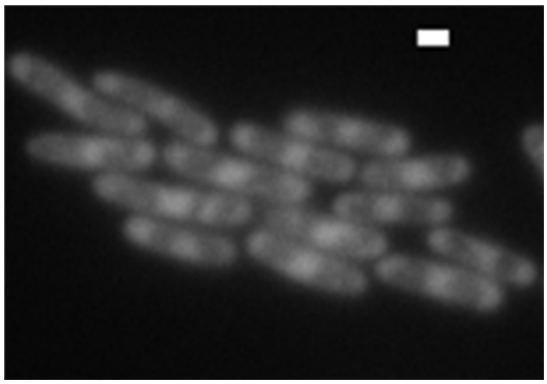

Figure S17. Fluorescence images of ribosome (S2-YFP) in cells grown on agar plate (Scale bar =1 μm).

References for Supporting Information

Bakshi, S., B. P. Bratton & J. C. Weisshaar, (2011) Subdiffraction-Limit Study of Kaede Diffusion and Spatial Distribution in Live Escherichia coli. *Biophys. J.* **101**: 2535-2544.

Biteen, J. S., M. A. Thompson, N. K. Tselentis, G. R. Bowman, L. Shapiro & W. E. Moerner, (2008) Super-resolution imaging in live Caulobacter crescentus cells using photoswitchable EYFP. *Nature Methods* **5**: 947-949.

Cheezum, M. K., W. F. Walker & W. H. Guilford, (2001) Quantitative comparison of algorithms for tracking single fluorescent particles. *Biophysical Journal* **81**: 2378-2388.

Mondal, J., B. P. Bratton, Y. Li, A. Yethiraj & J. C. Weisshaar, (2011) Entropy-Based Mechanism of Ribosome-Nucleoid Segregation in E. coli Cells. *Biophysical Journal* **100**: 2605-2613.

Otsu, N., (1979) Threshold Selection Method from Gray-level Histograms. *Ieee Transactions on Systems Man and Cybernetics* **9**: 62-66.

Rosenfel.A & J. L. Pfaltz, (1966) Sequential Operations in Digital Picture Processing. *Journal of the Acm* **13**: 471-&.

Sliusarenko, O., J. Heinritz, T. Emonet & C. Jacobs-Wagner, (2011) High-throughput, subpixel precision analysis of bacterial morphogenesis and intracellular spatio-temporal dynamics. *Mol. Microbiol.* **80**: 612-627.

Taniguchi, Y., P. J. Choi, G. W. Li, H. Y. Chen, M. Babu, J. Hearn, A. Emili & X. S. Xie, (2010) Quantifying E-coli Proteome and Transcriptome with Single-Molecule Sensitivity in Single Cells. *Science* **329**: 533-538.